MODELING OF JOULE HEATING AND THERMOELECTRIC TRANSPORT IN THIN FILM SILICON FOR SJEM MEASUREMENT

BY

YOUNGJOON KOH

THESIS

Submitted in partial fulfillment of the requirements
for the degree of Master of Science in Mechanical Engineering
in the Graduate College of the
University of Illinois at Urbana-Champaign, 2014

Urbana, Illinois

Adviser:

Professor William Paul King

ABSTRACT

This thesis reports the finite element modeling of a quantitative nanometer-scale temperature distribution along the doped Si devices. The modeling replicates data acquisition technique of Scanning Joule expansion microscopy (SJEM). Time varying heat equations and Maxwell's equations are solved in frequency domain and applied to commercial finite element software, COMSOL. Chapter 1 introduces various techniques to obtain nanoscale temperature distribution. In Chapter 2, Joule heating and Thermoelectric heating in 1^{st} harmonic and 2^{nd} harmonic signals are analyzed by comparing the terms in governing equations and simulation results. Chapter 3 optimizes device design of doped Si and experimental conditions for future measurement. The approach used in Chapter 2 is expanded in Chapter 4 to understand thermoelectric behaviors in 500 nm thick boron doped p-type and phosphorus doped n-type Si devices with doping levels of 10^{19} cm^{-3} and 10^{18} cm^{-3}. PtSi or NiSi Ohmic contacts are formed on the devices and thermoelectric behaviors are analyzed in conditions either under simultaneous DC and AC excitations, or AC only excitations. The simulation results show that thermoelectric contribution in heating increases with the product of electrical conductivity and Seebeck coefficient. Chapter 5 explains the future plan for the device fabrication and platform for contact resistance measurements. The studies in this thesis can extend to Schottky contact devices and further complicated structures for understanding heat and thermoelectric transport in specific frequency.

This thesis is dedicated to colleagues, my mother, my sisters and my father in the heaven.

ACKNOWLEDGMENTS

I would like to thank to my advisor, Professor William P. King for the opportunity to work in his group and guiding me on technical aspects of the project. I am grateful for his trust in my work during in master's degree. I would also like to thanks to my colleagues Kyle, Matt, Suhas, Sezer, Joon, Bikram, Huan and Joseph for valuable discussions and encouragement while working on this project. I would also like to thanks to my family for their endless support during my life. Special thanks to mechanical department of University of Illinois Urbana-Champaign for their resources and environment.

TABLE OF CONTENTS

CHAPTER 1: INTRODUCTION

The invention of Atomic Force Microscopy (AFM) enabled a detailed exploration of surfaces at micro and nanometer-scale [1]. AFM have led development of various scanning probe microscopes (SPMs) which can image topography and measure electronic, optical, thermal properties of material at nanometer-scale [2]. One of such techniques, scanning thermal microscopy (SThM) holds great potential to improve nanoelectronic devices since local hot spots in the device limits their advanced performances [3]. This thesis presents a detailed study of modeling of a quantitative nanometer-scale thermal measurement technique.

Energy transport in nanoscale materials can be observed by two major techniques. First, optical techniques such as photothermal spectroscopy and microscopy can measure temperature distribution at sub 500 nm spatial resolutions [4]. Using ultraviolet light provides a spatial resolution of about 100 nm, but imaging at higher resolutions requires breaking diffraction limits of light. The other major technique is SThM, which measures temperature distribution using the AFM cantilevers with integrated thermocouples or temperature sensors at cantilever tips [2]. These techniques have sub 100 nm spatial [4] and ~200 mK temperature resolution [5]. However for SThM, the spatial resolution is limited by the tip apex radius, which typically around ~50 nm. An alternate thermometry SThM technique is scanning Joule expansion microscopy (SJEM), which utilizes commercially available AFM cantilever [2, 6-8]. This condition enhances spatial resolution of technique, since the radius of cantilever tip is 1~5 nm and therefore enables ~10 nm spatial resolution measurement [7] with 250 mK temperature resolution. SJEM measures the thermal expansion signal of a sample using AFM and lock-in amplifier, and the temperature is extracted by converting the thermal expansion signal to temperature using finite element modeling. A thin

layer of polymer is deposited on sample to improve the thermal expansion signal and isolate electrostatic forces from AFM tips. SJEM is ideal for material characterization and energy transport measurement with high spatial and temperature resolution.

SJEM is useful for acquiring quantitative thermometry (temperature) and material properties especially for thin layers. Thermal conductivity of 43 nm-thick gold films has been measured using SJEM technique [7]. Studies on energy transport within 2D graphene sheets and phase change memory materials using SJEM have revealed thermoelectric powers and contact resistances between the device and metal contacts [9, 10]. However, energy transport in doped Si has not been investigated using SJEM technique. Thermoelectric powers of Si range from 100 μV/K to more than 1000 μV/K, and this large magnitude is expected to show different temperature behavior compare to material that has less than 100 μV/K.

This thesis describes the modeling of Joule heating (JH) and thermoelectric heating effects (TE) in doped Si channel to compare the thermal expansion in SJEM measurement. Joule heating and thermoelectric equations are solved in frequency domain and thermal expansion signal is observed in 1^{st} harmonic signals. Doped Si channel designs are optimized to minimize the error based on the numerical modeling results of SJEM measurement. 500 nm thick boron doped p-type and phosphorus doped n-type Si devices with doping levels of 10^{19} cm^{-3} and 10^{18} cm^{-3} are analyzed by comparing thermal expansion signals from Joule heating to thermoelectric effect. Metal contacts in the simulation are assumed as PtSi or NiSi Ohmic contacts to alleviate nonlinearity of total resistance change.

CHAPTER 2: MODELING OF SJEM

2.1 Device geometry

The device geometry built in COMSOL is based on SOI wafer. The device layer is 500nm thick, the oxide layer is 2 µm thick, and the handle layer is 200 µm thick. The width (w) of the metal contacts are modeled as 150 µm, depth (d) of the metal contacts as 150 µm, and thickness (t) as 100 µm. Since d is larger compare to channel length and thickness of device, 2D modeling was possible in the simulation. Separations between the two metal contacts can vary from 4 µm to 40 µm for actual devices. However, investigation of different channel lengths shows that the thermoelectric effect that occurs within the devices is not a function of channel length, as long as the device temperature is the same. This is explained in Figure 3.4.

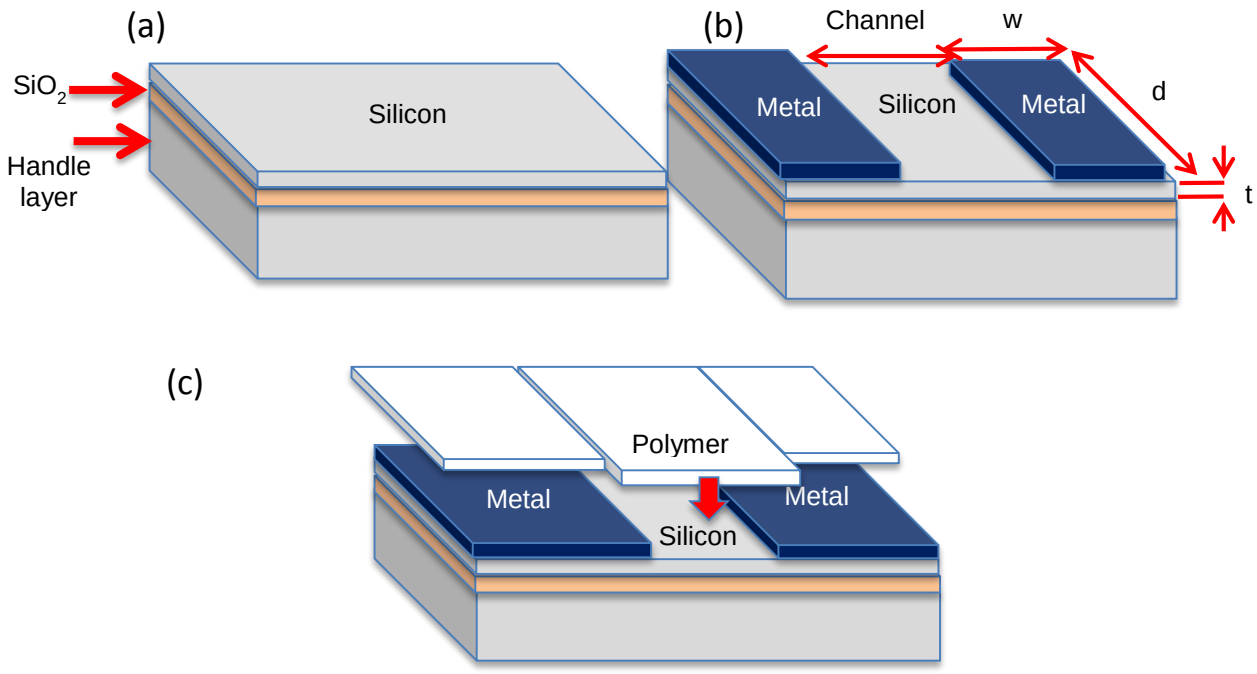

Figure 2.1 Device design in this simulation. (a) SOI wafer (b) Metal deposited on SOI wafer with 100nm thickness (c) Polymer deposition by either spin coating of polymer or parylene deposition machine.

2.2 Joule heating and Thermoelectric heating modeling

The thermoelectric effect is direct conversion of temperature difference to potential difference and vice versa. In order to include the thermoelectric effect in the Joule heating equation, heat diffusion and Maxwell equation must be solved simultaneously[11]. The time varying heat diffusion equation is

$$\rho C_p \frac{dT}{dt} + \nabla \cdot q = \dot{q} \qquad (1)$$

Here, ρ is density of material, C_p is heat capacity, T is temperature, q is energy density heat flux and $\dot{q}$ is energy generation. For Maxwell equation,

$$\nabla \cdot J = 0 \qquad (2)$$
$$E = -\nabla V \qquad (3)$$

where J is current density, E is electric field and V is electric potential. The related constitutive equations are

$$q = \pi \cdot J - k \cdot \nabla T \qquad (4)$$
$$J = \sigma \cdot (E - S \cdot \nabla T) \qquad (5)$$
$$\dot{q} = J \cdot E \qquad (6)$$

Where π stands for Peltier coefficient, $\pi = T \cdot S$, S stands for Seebeck coefficient, and k stands for thermal conductivity.

For the simulation, steady (DC) and a periodic (AC) voltage supplies are used in order to observe thermoelectric phenomena in different conditions. As a result, the temperature responses are in DC, 1st and 2nd harmonics. For simplicity, it is assumed that periodic supply and responses are all in cosine forms. In order to understand the thermoelectric effect within the devices, the Joule heating equation and the thermoelectric effect equations must be solved in frequency domain. First, Joule heating parts can be constructed from eq. (1) – (6) without considering thermoelectric effect. By collecting all equations together, the governing equations become

$$\rho C_p \frac{(T_{DC} + T_{1w} cos(2\pi f_0 t) + T_{2w} cos(4\pi f_0 t))}{dt} - \nabla \cdot [k\nabla\{T_{DC} + T_{1w} cos(2\pi f_0 t) + T_{2w} cos(4\pi f_0 t)\}] = \sigma[\nabla\{V_0 + V_1 cos(2\pi f_0 t)\}][\nabla\{V_0 + V_1 cos(2\pi f_0 t)\}] \quad (7)$$

$$\nabla \cdot [\sigma\nabla\{V_0 + V_1 cos(2\pi f_0 t)\}] = 0 \quad (8)$$

By performing Fourier transform on the equations,

$$\nabla \cdot \left[\begin{pmatrix} -k & 0_1 & 0 & 0 & 0 \\ 0 & -k & 0 & 0 & 0 \\ 0 & 0 & -k & 0 & 0 \\ 0 & 0 & 0 & \sigma & 0 \\ 0 & 0 & 0 & 0 & \sigma \end{pmatrix} \nabla \begin{pmatrix} T_0 \\ T_1 \\ T_2 \\ V_0 \\ V_1 \end{pmatrix} \right] = \begin{pmatrix} \sigma\{(\nabla V_0)^2 + \frac{1}{2}(\nabla V_1)^2\} \\ \sigma(2\nabla V_1 \nabla V_0) - i2\pi\rho C_p f_0 T_1 \\ \sigma\{\frac{1}{2}(\nabla V_1)^2\} - i2\pi\rho C_p 2 f_0 T_2 \\ 0 \\ 0 \end{pmatrix} \quad (9)$$

where $i=\sqrt{-1}$, f_0 is operating frequency. The top three rows are indicating heat diffusion equations and the bottom two rows are Maxwell equation. Eq. (9) shows that 1st harmonic temperature rise is expected when steady and periodic voltage sources are provided simultaneously.

$$\nabla \cdot \left[\begin{pmatrix} 2(k+\sigma S^2 T_0) & \sigma S^2 T_1 & \sigma S^2 T_2 & 2\sigma S T_0 & \sigma S T_1 \\ 2\sigma S^2 T_1 & \{2k + \sigma S^2(2T_0 + T_2)\} & \sigma S^2 T_1 & 2\sigma S T_1 & \sigma S(2T_0 + T_2) \\ 2\sigma S^2 T_2 & \sigma S^2 T_1 & 2(k+\sigma S^2 T_0) & 2\sigma S T_2 & \sigma S T_1 \\ \sigma S & 0 & 0 & \sigma & 0 \\ 0 & \sigma S & 0 & 0 & \sigma \end{pmatrix} \nabla \begin{pmatrix} T_0 \\ T_1 \\ T_2 \\ V_0 \\ V_1 \end{pmatrix} \right] = \begin{pmatrix} \sigma\{S(2\nabla T_0 \nabla V_0 + \nabla T_1 \nabla V_1) + 2(\nabla V_0)^2 + (\nabla V_1)^2\} \\ \sigma\{S(2\nabla T_0 \nabla V_1 + 2\nabla T_1 \nabla V_0 + \nabla T_2 \nabla V_1) + 4\nabla V_1 \nabla V_0\} - i4\pi\rho C_p f_0 T_1 \\ \sigma\{S(\nabla T_1 \nabla V_1 + 2\nabla T_2 \nabla V_0) + (\nabla V_1)^2\} - i4\pi\rho C_p 2 f_0 T_2 \\ 0 \\ 0 \end{pmatrix} \quad (10)$$

By including Seebeck and Peltier effect into eq. (9), the equation can be rearranged to similar form as eq. (10) [9]. Here, 3rd and 4th harmonic terms are ignored since their contribution is very small. Temperature dependent electrical conductivity of doped Si is linearly interpolated based on theory described in the literature [12] and coded in MATLAB for simulation purpose,

thanks to Prof. King in his Heat conduction class in UIUC. Data of Seebeck coefficients in doped Si were from [13] and thermal conductivities of doped silicon are extracted from [14].

2.3 Analytic approach for partial differential equations

It is important to understand how thermal signals are generated from the thermoelectric effect. Comparing thermal expansion from Joule heating and thermoelectric effects in certain harmonics gives clear view of how each phenomenon affects the temperature of the device. The second row of the Joule heating equations (eq. (11)) refers to the 1st harmonic of temperature, and they are a combination of applied voltage, material properties and time varying temperature. 1st harmonic thermal expansion by Joule heating is only allowed when DC and AC voltage sources are applied simultaneously. Therefore, no temperature rise is expected if either DC or AC voltage is zero. It is shown in Figure 2.2 (b).

$$\nabla \cdot (-k\nabla T_1) = \sigma(2\nabla V_1 \nabla V_0) - i2\pi\rho C_p f_0 T_1 \qquad (11)$$

On the other hand, thermoelectric effects in 1st harmonics are sensitive to AC voltage even if there is no DC supply. As shown in Figure 2.2(b) and (c), color plot indicates that measurable response appears in 1st harmonic without DC supply. In eq. (12), the right hand side (source term) contains values that are independent of DC and AC voltage products. (The equation is from the 2nd row of eq. (10).) Thermoelectric effect terms are a combination of Seebeck coefficient, electrical conductivity, steady and periodic terms. This produces thermo-mechanical response in 1st harmonic without DC supply, and is purely due to thermoelectric effect (eq. (12)). The comparison is shown in Figure 2.2. All the simulations here in Chapter 2.3 are based on p-type 10^{19} cm^{-3} devices.

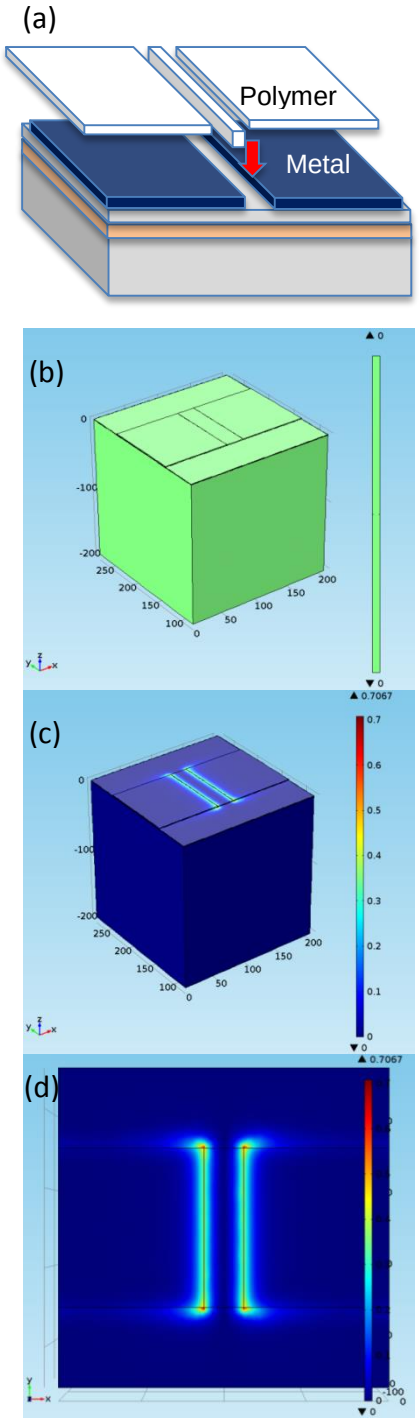

Figure 2.2 (a) Illustration of how the device is built, as shown in Chapter 2.1 (b) Temperature distribution in 1st harmonic signal. When only JH is considered in the simulation, no temperature rise is observed. (c) Thermal signal after TE is included in the equations (eq. (12)). Heating occurred due to Seebeck and Peltier effect. (d) Top view of the device. The color indicates absolute value of temperature within the device.

$$\nabla \cdot \left[\begin{matrix} \left(2\sigma S^2 T_1 \quad \{2k + \sigma S^2 (2T_0 + T_2)\} \quad \sigma S^2 T_1 \quad 2\sigma S T_1 \quad \sigma S (2T_0 + T_2)\right) \nabla \begin{pmatrix} T_0 \\ T_1 \\ T_2 \\ V_0 \\ V_1 \end{pmatrix} \end{matrix} \right] =$$

$$\left(\sigma\{S(2\nabla T_0 \nabla V_1 + 2\nabla T_1 \nabla V_0 + \nabla T_2 \nabla V_1) + 4\nabla V_1 \nabla V_0\} - i4\pi\rho C_p f_0 T_1\right) \quad (12)$$

This behavior is also can be observed in thermal expansion signal when magnitude of the AC voltage is fixed while DC voltage varies. In the simulation, thermal expansion signal can be obtained by introducing temperature rise into the solid mechanics module. Figure 2.3 is the case when DC voltage is swept from 0.4V to 0V, while amplitude of AC is fixed at 0.4V. The plots show absolute value of thermal expansion in 1st harmonic. When the device is subjected to DC 0.4V, thermo-mechanical behavior is exaggerated to one side as shown in Figure 2.3(b). This is because Peltier cooling is occurred at one end and heating at the opposite end. When DC supply is reduced to 0.1V, shape of thermal expansion signal starts to change. Lowest thermal expansion in the channel starts to occur inside of the channel. As DC voltage goes to zero, lowest thermal expansion appears in the center of the device channel. This transition is due to the change of the dominance in heating, from Joule heating to thermoelectric effect. The influence of Joule heating starts to decrease as the DC source reduces and Peltier effect becomes dominant in the device. As a result, the same thermal expansion magnitude can be observed when DC voltage becomes zero. When considering Joule heating only within the device, 1st harmonic signal does not show any thermal expansion. (Figure 2.3(c))

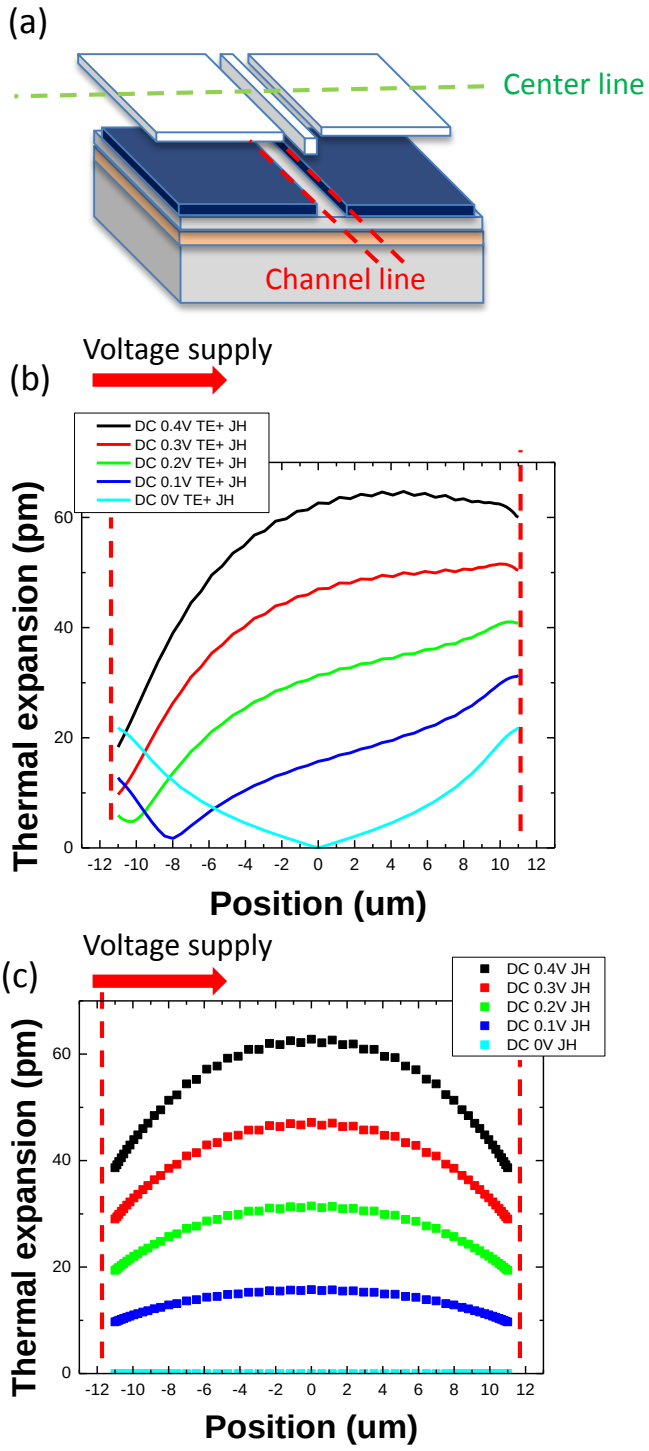

Figure 2.3 Thermal expansions in 1st harmonic. (a) The device is assumed to measure at the center of the device. Red line shows boundary of metal contacts, which is channel length. (b) Profile of thermal expansion with changing DC voltage (eq. (12)). Amplitude of AC voltage is fixed at 0.4V. The minimum thermal expansion moves into the channel as DC voltage becomes 0.1V. (c) Simulation results without thermoelectric effect included (eq. (11)). There are no thermal expansion signals when DC voltage is not provided.

It is also important to observe influence of power source in thermoelectric effect. When both DC and AC voltage increase simultaneously, the Joule heating term $4\nabla V_0 \nabla V_1$ in eq. (12) becomes larger than values associated with Seebeck coefficient. As a result, the position of peak expansion in the device starts to move closer to the center of device, which indicates dominance of Joule Heating (Figure 2.4(a)). This behavior can also be seen by looking at the thermal expansion ratio of TE to JH. Figure 2.4(b) shows that the contribution of the thermoelectric effect becomes smaller as voltage increases. The magnitude of voltages in the plot is amplitude. The TE to JH ratio is calculated by subtracting thermal expansion response of JH from JH + TE and dividing by JH thermal expansion response.

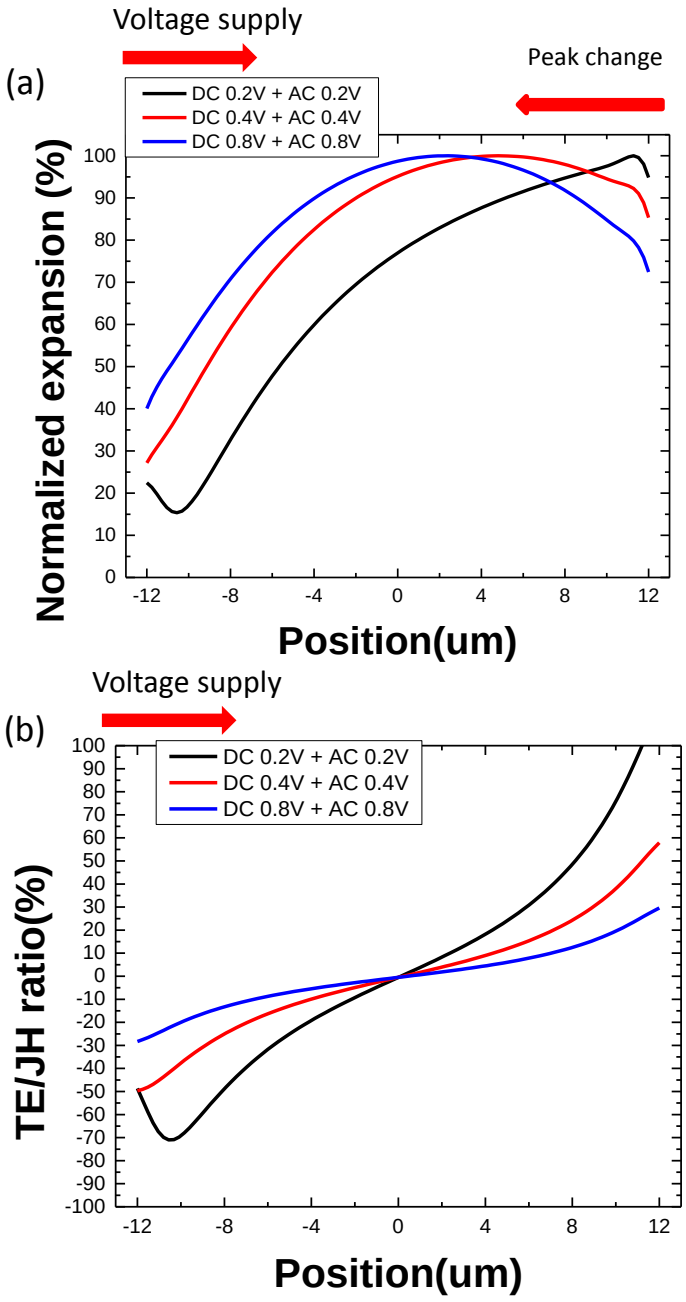

Figure 2.4 (a) Plot of normalized thermal expansion. As voltage increases, position of peak changes due to dominance of Joule Heating in the device. (b) TE/JH ratio with applied voltage change. This is simulated without contact resistance included. DC 0.2V + AC 0.2V case shows largest thermal expansion within the contact. This suggests that thermoelectric effect dominates Joule heating in the signal as applied voltage gets smaller.

2nd harmonic signals are analyzed by the same procedure. Although 3rd row of the matrix or 2nd harmonic equations in eq. (10) contains Seebeck coefficient in the equation, the results show that both JH + TE case and JH are very similar that they overlap each other (Figure 2.5). This is because the DC temperature contribution in the 2nd harmonic signal is very small compared to the 1st harmonic. This can be shown by comparing the source terms in eq. (12) and 3rd row of eq. (10). Since the 1st harmonic temperature in the source term of 3rd row of eq. (10) is also too small to produce appreciable thermoelectric effect in 2nd harmonic, it is possible to observe almost pure Joule heating response.

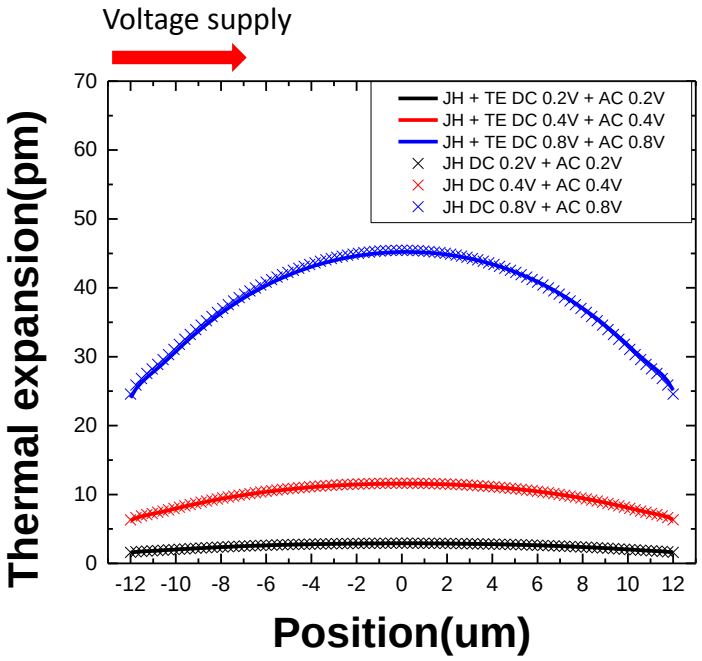

Figure 2.5 Thermal expansion profiles in 2nd harmonic signal. Due to the strong Joule Heating signal, no difference is shown between JH + TE and JH cases.

CHAPTER 3: OPTIMIZATION

3.1 SJEM technique

The SJEM technique, as shown in figure 3.1, employs an AFM and lock-in amplifier to measure temperature distributions in the sample with sub-100 nm spatial resolution. Similar to the operation mechanism for topography imaging, AFM can measure thermal expansion signals when the sample is subjected to current or voltage sources. Thermal expansion of the sample induces cantilever deflection, while the laser is focused on the backside of cantilever. The cantilever deflection is measured by following the bounced laser using a photodiode. While AFM scans the sample substrate, the AFM feed-back loop monitors the photodiode and piezoelectric stage to maintain a constant tip-substrate contact force. A lock-in amplifier collects thermal expansion data in terms of magnitude and phase at certain frequency. As polymers have high thermal expansion coefficient values, a thin polymer coating on sample amplifies thermal expansion signals. In addition, the polymer coating protects the cantilever from electrostatic force.

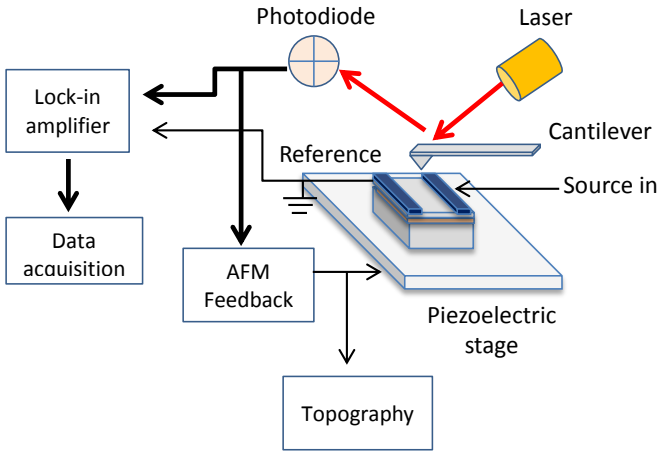

Figure 3.1 Schematic of SJEM technique. A power source applies voltage or current to the device while a cantilever scans the device substrate. Cantilever deflection is detected by a photodiode while the thermal expansion signal is locked in at certain frequency. The AFM feedback loop controls the piezoelectric stage.

3.2 Optimization of device geometry and measurement condition

This section describes the optimization process of device geometry and measurement conditions, in order to observe the maximum thermoelectric effect of the samples. As explained in the previous chapter, the heating contribution from the thermoelectric effect can be realized by

$$(Ex_{JH+TE} - Ex_{JH}) \Big/ Ex_{JH} \qquad (13)$$

Here, the *Ex* is absolute magnitude of thermal expansion and subscript *JH + TE* and *JH* are cases when Joule heating and thermoelectric effects are considered together or only Joule heating, respectively. The voltage source condition can be either in only periodic or periodic with DC offset, and appreciable thermoelectric effects can be seen in 1st harmonic signal, as described in Chapter 2.3. Figure 3.2 shows one of the examples of thermal expansion in *JH* or *JH + TE* case. Plots in Figure 3.2 do not contain heating from contact resistance. In Figure 3.2, thermal expansion profiles of p-type (Figure 3.2 (a)) and n-type (Figure 3.2 (b)) are in opposite direction, which indicates the difference in signs of Seebeck coefficient. A TE to JH ratio is almost symmetric from the center of device channel (where the position is at 0), which indicates that the contribution of thermoelectric effects in the devices are equally distributed. Each device shows ~ 10% higher TE/JH ratio at one end of channel compare to the other end. Since the electrical conductivity of doped Si decreases with temperature increment [12], the phenomenon may stem from the difference in electrical conductivities at the contacts. Decreased electrical conductivities at higher temperatures can reduce thermoelectric effect. However, the highest TE to JH ratio in each sample is occurred at the end where temperature is higher. Variables in TE included equations (eq. (12)) are closely related to each other and therefore it is difficult to simply assume that this phenomenon is from one of variables.

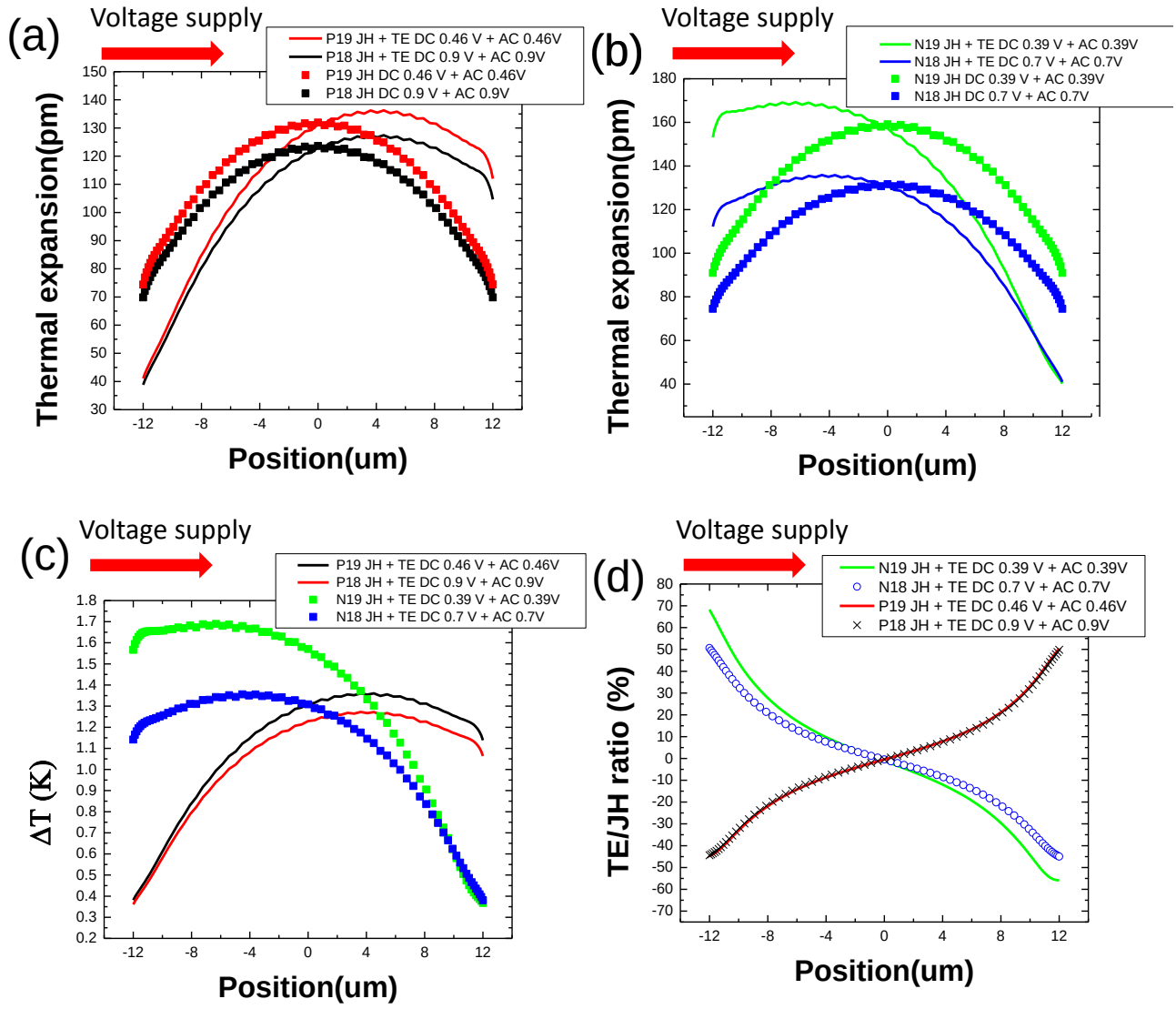

Figure 3.2 1st harmonic thermal expansion profiles from JH and JH+TE case for (a) p-type and (b) n-type devices. P and N stand for p-type and n-type, 19 and 18 are $10^{19}cm^{-3}$ and $10^{18}cm^{-3}$.(c) Comparison of temperature rise of JH + TE case for p and n-types. (d) TE/JH ratio of p and n-type cases. TE/JH ratios are almost symmetric but ~10 % higher at one end.

Thermal expansion data acquired from SJEM may have intrinsic error when the sample expands less than 100 pm. It has been observed that SJEM have 2 pm errors when measuring the samples at fixed position for more than 20 repeated times. Therefore, the intrinsic error is larger than 2 % for if thermal expansion in the sample is less than 100 pm. However, thermoelectric effect contribution in 1st harmonic heating becomes larger when the input voltage reduces, as shown in Figure 2.4. In this sense, there are optimized voltage magnitudes in order to see large thermoelectric effect with small measurement errors. In this simulation, the voltage supply condition was set to have minimum 40 pm thermal expansion within the device, which produces maximum error of 5%. All the simulation results in Chapter 3 and Chapter 4 are assumed to have minimum thermal expansion of 40pm.

Important factor for device design is the channel length. From Ohm's law, resistance of the device increases as the channel, which is an electrical path, become longer. According to the discussion above and Figure 2.4, heating from the thermoelectric effect is amplified when the applied voltage is small and therefore the shorter channel length is desired. However, designated voltage may not be applied to the samples if unkown impedence from electronic packaging and metal contacts are large. Contribution of such unknown sources reduces the accuracy in SJEM measurement and simulation results. In this sense, the device resistance requires to be high enough to alleviate the error arising from unknown impedence sources. Assuming that the maximum resistance of unknown equipment set ups is 1 Ω, the device resistance around 20 Ω is preferable to keep measurement errors below 5%. From this aspect, doping level values of 10^{19} cm^{-3} and 10^{18} cm^{-3} are chosen for both p and n-type devices. Resistances for 10^{19} cm^{-3} p-type and n-type Si devices with 24 μm long channels are calculated based on the geometry presented in Chapter 2.1, which corresponds to 24 Ω and 18 Ω, respectively. Devices at the dopoing level of 10^{17} cm^{-3} and

lower impurity concentrations are ignored because of low electrical conductivity. It is expected to have large thermoelectric effects in 1st harmonic when the product of electrical conductivity and Seebeck coefficients is large. More detailed analysis on this is presented in Chapter 4. Therfore, the presented simulation results for Si devices with the channel length of 24 μm or higher is accurate with the maximum error of 5%.

However, the thermoelectric effect within devices is not directly related to the channel length, as shown in figure 3.3. It is because the channel length does not change the electrical conductivity or Seebeck coefficient of the devices. From this aspect, when temperature at the metal contacts are managed to have a same value, the maximum thermal expansion TE/JH ratio remains same regardless of the channel length. Therefore, the simulated temperature distribution for the device with 24 μm channel length should be same for the devices with different channel lengths under identical doping conditions.

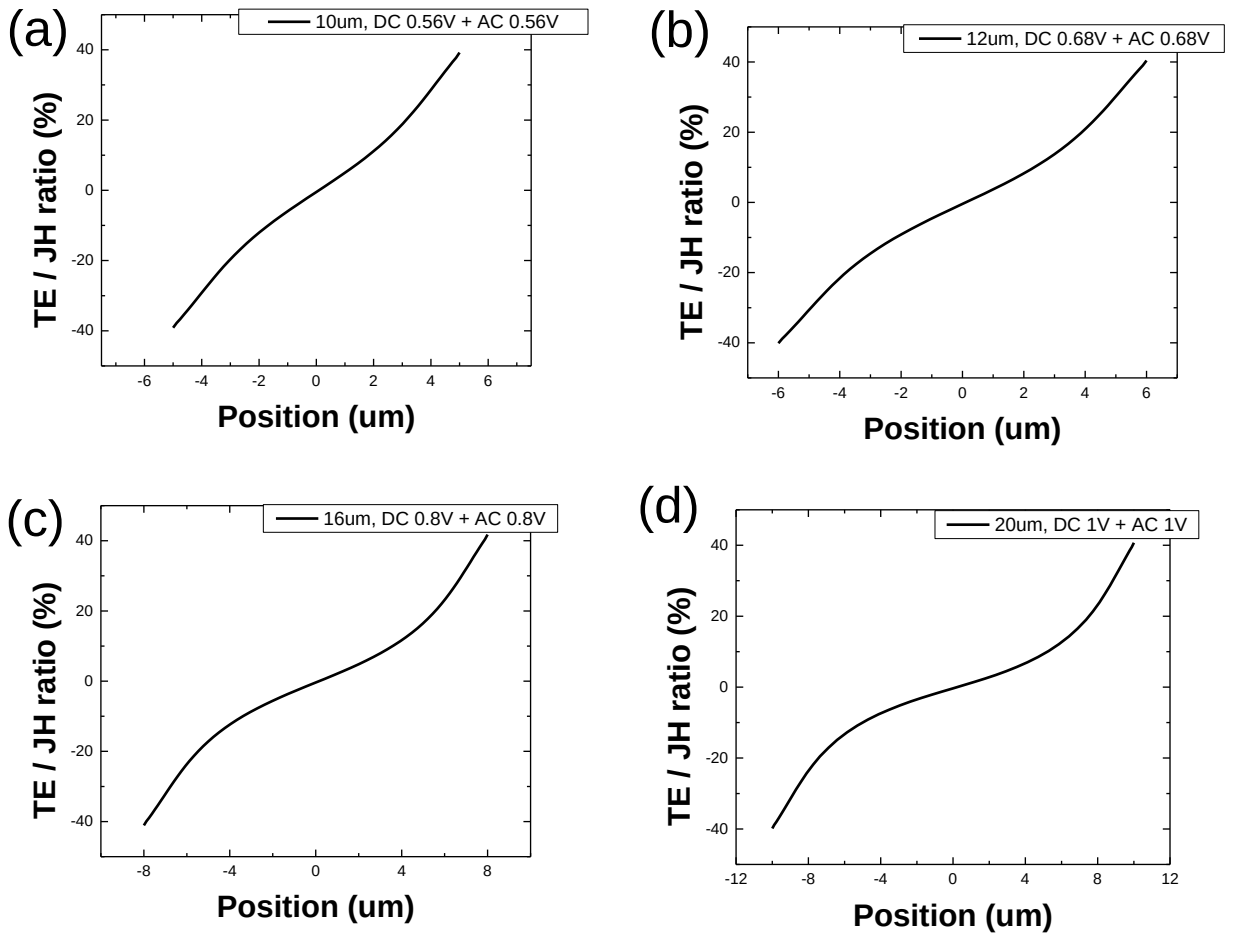

Figure 3.3 $10^{19}cm^{-3}$ p-type is simulated for TE/JH ratio comparison. The ratio is a function of position across the devices with various channel lengths of (a) 10 µm, (b) 12 µm, (c) 16 µm, (d) 20 µm. For all cases, the maximum TE/JH ratios are same at about 40%. All devices are simulated at same excitation frequency of 27 kHz. Inserted applied voltage describes the maximum amplitude when DC and AC voltages are applied simultaneously.

Resistance of electrical contacts induces non-negligible power dissipation for the Si devices. Especially, when the resistance of electrical contacts is nonlinear with applied voltage, matching SJEM measurements and simulation results is challenging. In order to reduce the complexity in both simulations and measurements, the devices are assumed to form Ohmic contact with Si devices. It has been reported that the Ohmic contact can be built by forming PtSi or NiSi. Contact resistivity data of such silicides with varying doping concentrations of silicon is reported in previously published literatures [15, 16]. Transmission line method (TLM) [17], four-point probe measurement, and Van der Pauw structure [18] is used to accurately extract the total resistances and specific contact resistances. Table 3.1 shows the calculated contact resistance under following assumptions: 1) contact resistivity is same as reported in [15], 2) larger metal contact length of 200 μm compared to the transfer length, and 3) the sheet resistance of Si is consistent regardless of the distance from the metal contact. From simulation, it is calculated that 50% of Joule heating due to contact resistance is dissipated into the contact area while the other 50% of heating penetrates into the device.

Table 3.1 Contact resistance for different doping levels and types of metals are calculated.

	Specific contact resistivity (Ω-cm^2)	Sheet resistance (Ω/sq)	Transfer Length (μm)	Contact resistance (Ω)
1e19 p-type PtSi	1E-07	176.2	0.01065	0.06637
1e18 p-type PtSi	2E-04 (*)	816	0.04950	1.428286
1e19 n-type PtSi	1E-04	108.7	0.42894	1.648484
1e18 n-type PtSi	2E-01 (*)	450	2.10818	33.54102
1e19 p-type NiSi	1E-05	176.2	0.10653	0.663702
1e18 p-type NiSi	2E-02 (*)	816	1.56556	45.16636
1e19 n-type NiSi	1E-06	108.7	0.04289	0.164848
1e18 n-type NiSi	2E-03(*)	450	0.66666	10.6066

(*) These numbers are not shown in the reference. Therefore assume to be 500 times larger than 10^{19}cm^{-3} for PtSi and NiSi contact. The calculation of contact resistance is based on empirical results [15, 16]

CHAPTER 4: SIMULATION RESULTS

In order to understand the impact of dopant concentration on thermoelectric effect (TE) in silicon, two different cases are considered. First case is the simultaneous application of DC and AC voltages to the devices. For a systematic comparison of the thermoelectric effect in terms of the 1st harmonic signal, voltages are adjusted to obtain a minimum thermal expansion (TE) of 40 pm for each device. DC and AC voltages are applied with frequency of 63 kHz. Total voltage magnitude changes from 0V to two times of the DC voltage in the plot. The 1 μm thick Parylene C is deposited on the sample in this simulation.

Figure 4.1 shows the simulation results in terms of the temperature rise as a function of position along the channel length. Corresponding ratio of TE to JH is also provided. Figure 4.1(a) and (b) show that the 40 pm thermal expansion corresponds to a temperature rise of 0.7 K in the 1st harmonic signal, regardless of the metal contacts and doping type (mass density and heat capacity of doped Si does not vary with doping concentration in this simulation). Figure 4.1 (c) and (d) show that dopant concentration of 10^{19} cm^{-3} results in larger TE/JH values when compared to the 10^{18} cm^{-3} cases for both p and n-type devices. This is due to the larger product of electrical conductivity and Seebeck coefficient for the highly doped devices, resulting in a smaller voltage requirement for the 0.7 K temperature rise. Decreasing the voltage input to the device reduces relative contribution of the Joule heating, but increases the thermoelectric effect. This phenomenon is due to the source terms in eq. (12) in Chapter 2.3. Smaller improvements of TE/JH ratio in p-type compare to n-type with increased doping concentration is due to the less improvement in the product of electrical conductivity and Seebeck coefficient compare to that of n-type (figure 4.1 (c) and (d)).

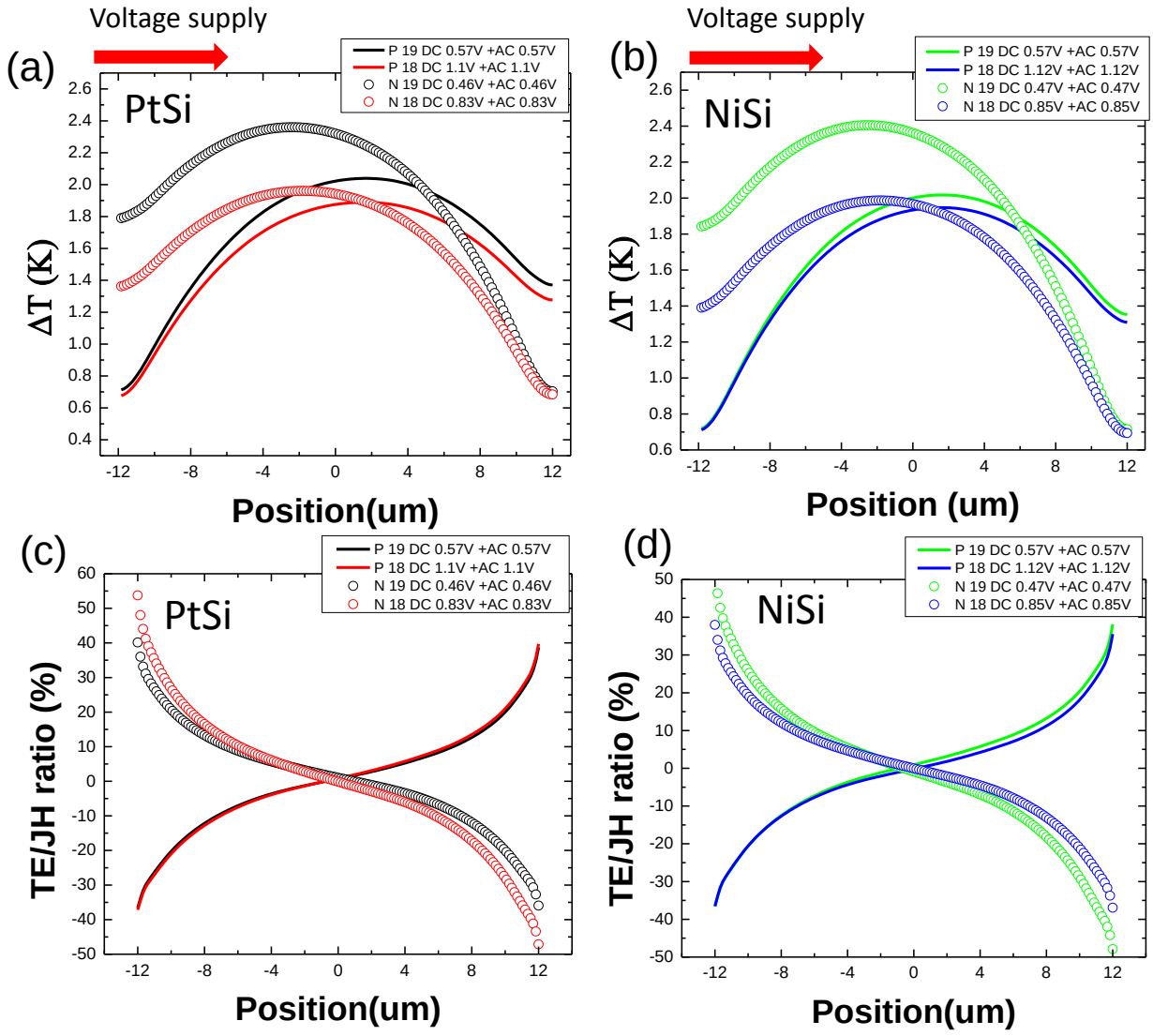

Figure 4.1 Simulation results of PtSi and NiSi contacts for different dopant concentrations. P 19 and N 19 stand for 10^{19} cm^{-3} p-type and 10^{19} cm^{-3} n-type. (a) 1st harmonic temperature rise for PtSi device. Both p-type and n-type devices have a minimum temperature rise of 0.7 K, which corresponds to a thermal expansion of 40 pm. (b) 1st harmonic temperature rise for NiSi device. (c) Ratio of TE to JH for PtSi contact. (d) Ratio of TE to JH for NiSi contact.

In addition to combined AC and DC voltages, dopant concentration and thermoelectric effect relationship is also analyzed by applying AC voltage without DC offset. Figure 4.2 shows that when DC component is removed, 1st harmonic temperature rise occurs due to the thermoelectric effect (see eq. (12)). The comparison of figure 4.2(a) and (b) shows that the n-type devices with the PtSi contacts show larger temperature rise when compared to NiSi case. This is same for the previous case (Figure 4.1 (c) and (d)) that the n-type devices with PtSi contacts result in ~10% larger TE/JH values than NiSi case.

In both Figures 4.1 and 4.2, Peltier effect is the dominant mechanisms at the metal contact compared to the Joule heating. Since the heat capacity of the contact determines the temperature rise, contribution of the thermoelectric effect is dominated by the material properties. Heat capacity of Pt is smaller than Ni, and as a consequence, the TE/JH value for PtSi is larger than the NiSi case. Overall, for the same doping concentration, n-type devices have larger maximum TE/JH ratio due to the product of electrical conductivity and Seebeck coefficients being smaller than the p-type case.

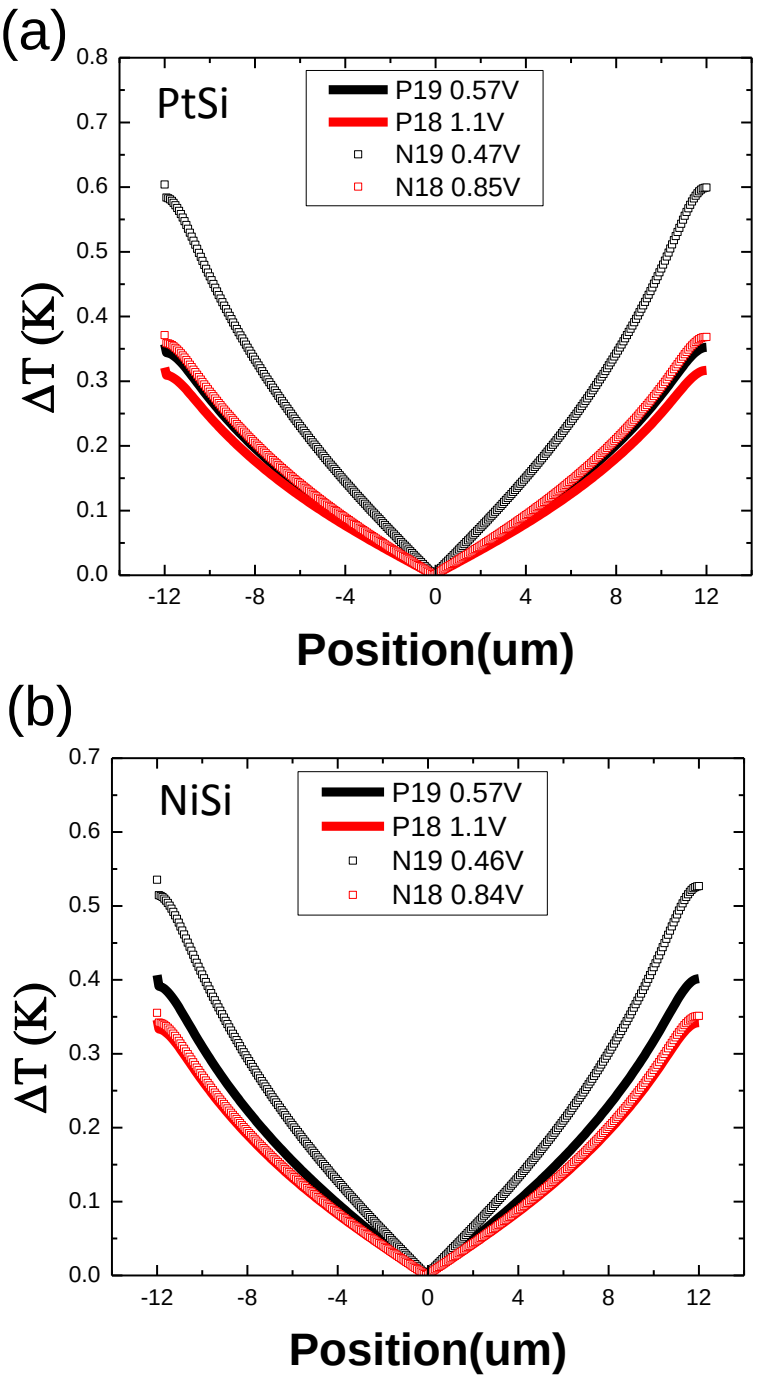

Figure 4.2 For p-type devices, the difference between 10^{19} cm^{-3} and 10^{18} cm^{-3} cases is small, while the corresponding difference for n-type devices is much larger. This is due to the small improvements in the product of electrical conductivity and Seebeck coefficient. (a) Temperature rise of PtSi contact in1st harmonic without DC voltage. (b) Temperature rise of devices with NiSi contacts in 1st harmonic without DC voltage.

CHAPTER 5: CONCLUSION

5.1 Future work

This section proposes the design and fabrication of doped silicon. The device will be fabricated using a double side polished SOI wafer with a 0.5 µm thick device layer, 2 µm thick silicon oxide layer, and a 500 µm thick handle layer will be used. Figure 5.1 shows the components that will be constructed on the masks. Figure 5.1 (a) illustrates device structure for SJEM measurements. The size of 200 µm X 200 µm metal contacts will simply be deposited on to the doped Si. The distance between a pair of metal pads will be varied from 4 µm to 40 µm. Adjacent devices will be electrically isolated from each other by etching a trench around the periphery of each device. In order to measure contact resistance of metals on the device, TLM bars are presented (Figure 5.1 (b)). 200 µm X 200 µm metal contacts will be used again on TLM bars, which will make easy to match the contact resistance measured from TLM bars to the actual doped devices. The calculation of contact resistance using TLM is described in the literature [17]. Four-point probe measurement will be performed on the rectangular bar in Figure 5.1 (c). This technique can extract 1) Sheet resistance of doped Si 2) Electrical conductivity of contact metals. Van der Pauw technique is another way to extract sheet resistance of the materials. A typical Greek cross structure is shown in Figure 5.1 (d). The sheet resistance is determined by forcing current from pad A to B and measuring the potential difference across D and C [19].

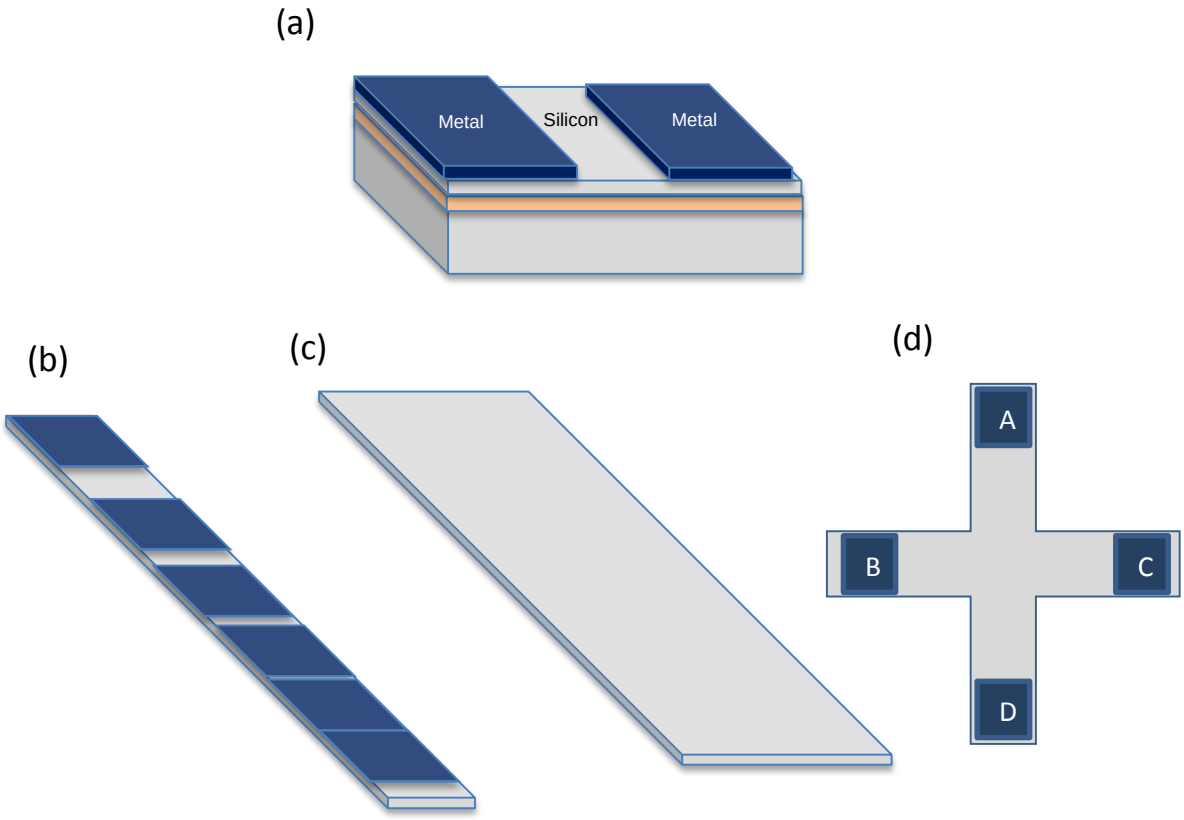

Figure 5.1 The CAD design of mask designs for future fabrication. (a) Doped Si devices for SJEM measurement. The distances of between metal contacts in the devices vary from 4 µm to 40 µm. (b) TLM bar for contact resistance measurement. The metal pad size is 200 µm by 200 µm. The distance between pads will vary from 5 µm to 100 µm. (c) Measurement bar for Four-point probe. The longer and shorter lengths are 4.5 mm and 1.5 mm, respectively. (d) The greek structure of Van der pauw for complementary of TLM method.

5.2 Summary

This thesis reports an investigation of the temperature distribution in a thin film doped silicon device using finite element analysis. Silicon devices with 10^{19} cm^{-3} and 10^{18} cm^{-3}, p and n-type devices are considered. When doping concentration is increased in the devices, contribution of thermoelectric heating compare to Joule heating is enhanced because of the improvement in product of electrical conductivity and Seebeck coefficients. In both DC + AC voltage case and AC voltage only case, PtSi Ohmic contact showed larger maximum TE/JH ratio compare to NiSi Ohmic contact case. Figure 4.1 and 4.2 prove that heat capacity of the contact material determines the maximum TE/JH ratio.

APPENDIX A

Sentaurus TCAD Code

```
line x location=0.0     spacing=  1<nm> tag=SiTop
line x location= 10<nm> spacing=  2<nm>
line x location= 50<nm> spacing= 5<nm>
line x location=100<nm> spacing= 20<nm>
line x location=500<nm> spacing= 50<nm> tag=SiBottom

region Silicon xlo=SiTop xhi=SiBottom
init concentration=8.0e14<cm-3> field=Boron
mgoals min.normal.size=3<nm> max.lateral.size=0.05<um> normal.growth.ratio=1.4

gas_flow name=O2_1_N2_1 pressure=1<atm> flowO2=1.2<l/min> flowN2=1.0<l/min>
diffuse temperature=900<C> time=40<min> gas_flow=O2_1_N2_1
select z=1
layers

implant Boron energy=120<keV> dose=5.1E14<cm-2> tilt=45<degree> rotation=0<degree>

SetPlxList { BTotal }
WritePlx noannealboron.plx

diffuse temperature=1100<C> time=50<min>
strip Oxide

SetPlxList { BTotal}
WritePlx boron.plx
```

APPENDIX B

Material properties in the simulation

Heat and thermoelectric transport part

	Electrical conductivity (S/m)	Mass density (kg/cm^3)	Heat capacity (J/(kg*K))	Thermal conductivity (W/(m*K))	Seebeck coefficient (V/K)
SiO_2	1E-24	2200	730	1.4	1E-34
Handle layer (Si)	1E-18	2300	700	149	1E-28
Parylene C	1E-7	1289	712	0.084	1E-18
Pt	8.9E6	21450	133	71.6	-5.28E-6
Ni	13.8E6	8900	445	90.7	-19.5E-6
10^{19} p-type	293.15 K :11600 370 K :9809	2300	670	100	0.5E-3
10^{18} p-type	293.15 K :2567.7 370 K :1995	2300	670	100	1E-3
10^{19} n-type	293.15 K :18446.6 370 K :16203.2	2300	670	100	-0.6E-3
10^{18} n-type	293.15 K :4523 370 K :3828.9	2300	670	100	-0.8E-3

Thermo-mechanical part

	Thermal expansion coefficient (1/K)	Mass density (kg/cm^3)	Young's modulus (Pa)	Poisson's ratio
SiO_2	0.5E-6	2200	70E9	0.17
Handle & Device layer (Si)	2.6E-6	2300	170E9	0.28
Parylene C	35E-6	1289	2.579E9	0.4
Pt	8.8E-6	21450	168E9	0.38
Ni	13.4E-6	8900	219E9	0.31

REFERENCES

[1] G. Binnig, *et al.*, "Atomic force microscope," *Physical review letters,* vol. 56, p. 930, 1986.

[2] J. Varesi and A. Majumdar, "Scanning Joule expansion microscopy at nanometer scales," *Applied Physics Letters,* vol. 72, pp. 37-39, 1998.

[3] E. Pop, "Energy dissipation and transport in nanoscale devices," *Nano Research,* vol. 3, pp. 147-169, 2010.

[4] A. Majumdar, "Scanning thermal microscopy," *Annual review of materials science,* vol. 29, pp. 505-585, 1999.

[5] G. Wielgoszewski, *et al.*, "Microfabricated resistive high-sensitivity nanoprobe for scanning thermal microscopy," *Journal of Vacuum Science & Technology B,* vol. 28, pp. C6N7-C6N11, 2010.

[6] A. Majumdar and J. Varesi, "Nanoscale temperature distributions measured by scanning Joule expansion microscopy," *Journal of Heat Transfer,* vol. 120, pp. 297-305, 1998.

[7] S. P. Gurrum, *et al.*, "Size effect on the thermal conductivity of thin metallic films investigated by scanning Joule expansion microscopy," *Journal of Heat Transfer,* vol. 130, p. 082403, 2008.

[8] M. Cannaerts, *et al.*, "Calibration of a scanning Joule expansion microscope (SJEM)," *Applied Physics A,* vol. 72, pp. S67-S70, 2001.

[9] K. L. Grosse, *et al.*, "Nanoscale Joule heating, Peltier cooling and current crowding at graphene-metal contacts," *Nat Nano,* vol. 6, pp. 287-290, 2011.

[10] K. L. Grosse, *et al.*, "Direct observation of nanometer-scale Joule and Peltier effects in phase change memory devices," *Applied Physics Letters,* vol. 102, p. 193503, 2013.

[11] M. Jaegle, "Multiphysics Simulation of Thermoelectric Systems-Modeling of Peltier-Cooling and Thermoelectric Generation," in *COMSOL Conference 2008 Hannover*, 2008.

[12] S. Reggiani, *et al.*, "Electron and hole mobility in silicon at large operating temperatures. I. Bulk mobility," *Electron Devices, IEEE Transactions on,* vol. 49, pp. 490-499, 2002.

[13] T. Geballe and G. Hull, "Seebeck effect in silicon," *Physical Review,* vol. 98, p. 940, 1955.

[14] M. Asheghi, *et al.*, "Thermal conduction in doped single-crystal silicon films," *Journal of Applied Physics,* vol. 91, pp. 5079-5088, 2002.

[15] N. Stavitski, *et al.*, "Systematic TLM measurements of NiSi and PtSi specific contact resistance to n-and p-type Si in a broad doping range," *Electron Device Letters, IEEE,* vol. 29, pp. 378-381, 2008.

[16] N. Stavitski, *et al.*, "Evaluation of transmission line model structures for silicide-to-silicon specific contact resistance extraction," *Electron Devices, IEEE Transactions on,* vol. 55, pp. 1170-1176, 2008.

[17] G. Reeves and H. Harrison, "Obtaining the specific contact resistance from transmission line model measurements," *Electron Device Letters, IEEE,* vol. 3, pp. 111-113, 1982.

[18] L. Van der Pauw, "A method of measuring the resistivity and Hall coefficient on lamellae of arbitrary shape," *Philips technical review,* vol. 20, pp. 220-224, 1958.

[19] S. Enderling, *et al.*, "Sheet resistance measurement of non-standard cleanroom materials using suspended Greek cross test structures," *Semiconductor Manufacturing, IEEE Transactions on,* vol. 19, pp. 2-9, 2006.